Corrosion Science 261 (2026) 113582

Contents lists available at ScienceDirect

Corrosion Science

journal homepage: www.elsevier.com/locate/corsci

Comparing the oxidation behaviour of three generations of single crystal nickel-based superalloys at an intermediate service temperature

Joseph C. Doyle [a,*], Edward A. Saunders [b], Jane M. Woolrich [c], Mark E. Light [d], Nong Gao [a], Philippa A.S. Reed [a]

[a] Engineering Materials Research Group, School of Engineering, University of Southampton, Southampton SO17 1BJ, UK
[b] Rolls-Royce plc., Materials – Failure Investigation, Bristol BS34 7QE, UK
[c] Rolls-Royce plc., Materials – Failure Investigation, Elton Road, Derby DE24 8BJ, UK
[d] School of Chemistry and Chemical Engineering, University of Southampton, Southampton SO17 1BJ, UK

ARTICLE INFO

Keywords:
Ni-based superalloys
Single crystal
Oxidation
Oxidation kinetics
Intermediate temperature
Oxidation mechanism

ABSTRACT

The oxidation behaviours of three different generations of single crystal Ni-based superalloys (SRR-99 – 1st generation, CMSX-4 – 2nd generation, and CMSX-10N – 3rd generation) have been investigated and compared at 550 °C. Isothermal oxidation tests were carried out at various exposure times ranging from 2 h up to 1000 h and it was found that oxide morphology and development showed noticeable differences between the alloys. Scanning electron microscopy (SEM), 3D imaging reconstruction, energy-dispersive X-ray spectroscopy (EDS) and X-ray diffraction (XRD) were employed to characterise the oxide scales. The external and internal oxides were studied through high-resolution imaging, measurements from which revealed the oxidation kinetics of CMSX-4 and CMSX-10N followed a near-parabolic law whilst a logarithmic law better described the kinetics behaviour of SRR-99. Thermodynamic modelling was used to predict the species and composition of oxides formed in each alloy and compared to measured EDS and XRD results. From the experimental results and modelling, it was found that the mechanism and oxide products formed for CMSX-4 and CMSX-10N are very similar, as NiO initially formed externally over the γ channels and the γ' precipitates were preferentially oxidised internally at the γ/γ' interface.

1. Introduction

Gas turbine technology is primarily implemented in jet propulsion and power generation systems, and nearly a century after first use in industry, there continue to be advancements in this technology to improve performance and reliability. Since the first gas turbine conception in the 1930s, a main driving force in improving the performance was increasing efficiency which is directly linked to increasing the combustion temperature [1,2]. These days the turbine entry temperature (TET) is typically in the range of 1400 °C-1500 °C [3]; however, the most recent developments in aeroengine designs are able to operate with a significantly higher TET, assisted by advanced cooling technology [4]. Single crystal superalloys have been found to be the best choice of alloy to cope with the extreme combination of high temperature and centrifugal stress in the turbine section of the aeroengine. This is due to the lack of grain boundaries within the blade, enhancing creep resistance at elevated temperatures. However, as the operating temperature continues to increase, degradation due to oxidation and hot corrosion is unavoidable; therefore, thermal barrier coatings (TBCs) are applied to help protect the blades in the hottest parts of the engine. Where the blade experiences intermediate temperatures, (i.e. in the blade shank close to the blade fir tree root or cooling channels) the blade is often left uncoated by the TBC due to assembly issues thus reducing the protection against oxidation damage to the underlying alloy. As a result, understanding the oxidation behaviour of superalloys at these intermediate temperatures and the potential implications on turbine blade failures is of great importance.

Ni-based superalloys gain their high temperature oxidation resistance from the formation of passive protective oxides that are thermally stable, adherent to the substrate and limit the diffusion of oxygen to the inner surface [5–7]. The main contributing elements to the formation of protective oxides are aluminium (Al) and chromium (Cr) through the growth of alumina (α-Al_2O_3) and chromia (Cr_2O_3) scales respectively [7–9]. Extensive research on the high temperature (>800 °C) oxidation

---

* Corresponding author.
E-mail address: j.c.doyle@soton.ac.uk (J.C. Doyle).

https://doi.org/10.1016/j.corsci.2025.113582
Received 11 November 2025; Received in revised form 15 December 2025; Accepted 25 December 2025
Available online 26 December 2025
0010-938X/© 2026 The Authors. Published by Elsevier Ltd. This is an open access article under the CC BY license (http://creativecommons.org/licenses/by/4.0/).

behaviour of superalloys exists [10–13]; whereas there is limited published work on the oxidation of superalloys at intermediate temperatures (450 °C-650 °C). Although oxidation reactions and formation will be slower at these intermediate temperatures, the formation of the passive protective oxides (α-Al_2O_3 and Cr_2O_3) can be restricted, potentially causing more severe oxidation than would be otherwise expected. This has been shown by Li *et al.* [13] where it was found that oxidation growth was slower at 900 °C than 800 °C for a single crystal superalloy due to the formation of a protective α-Al_2O_3 at 900 °C, which didn't form at 800 °C.

Alongside the development of the aeroengine, single crystal (SX) superalloys have also evolved through different generations to keep up with the ever-increasing demand for a higher TET. Generally, for each new generation of SX superalloys there is a higher composition of rhenium (Re) and other refractory elements compared to the previous generation, which can greatly improve the creep resistant properties of the superalloy allowing it to operate at higher service temperatures. However, this increase in creep resistance improving elements often comes with the compromise of reduced levels of elements that aid in oxidation resistance such as Cr [14]. This is since both Re (and other refractory elements) and Cr can cause the precipitation of deleterious topologically close-packed (TCP) phases, so as the Re content is increased in later generation alloys, the Cr content must be decreased [8]. In this study therefore the oxidation behaviour of three different generations of single crystal superalloys is compared: SRR-99, CMSX-4 and CMSX-10N, which are first, second and third generation superalloys respectively.

The aim of this study then is to evaluate the oxidation behaviour of different generations of SX superalloys under isothermal conditions at 550 °C through a combination of scanning electron microscopy (SEM), energy dispersive X-ray spectroscopy (EDS) and 3D stereoscopic image reconstruction techniques to gain understanding of the oxidation species forming and their kinetics at an intermediate service temperature.

2. Experimental procedures

2.1. Materials and characterisation techniques

The materials tested in this study are single crystal superalloys SRR-99, CMSX-4 and CMSX-10N, which have been provided by Rolls-Royce plc, in the form of cylindrical bars of 9.5 mm diameter and roughly 60 mm in length, all of which have received a proprietary commercial heat treatment. The nominal composition of each alloy is shown in Table 1; notably SRR-99 contains no Re and 8.5 wt% Cr, CMSX-4 contains 3.0 wt% Re and 6.5 wt% Cr, and finally CMSX-10N contains 6.8 wt % Re and 1.6 wt% Cr. This shows the trade-off in higher Re content for a lower Cr content in each new iteration of superalloys.

Microstructural characterisation was performed on the cut-offs of the cylindrical bars by sectioning into smaller coupons and preparing using a standard metallographic process of grinding and polishing, finishing with a 1μm diamond suspension. The polished coupons were etched to reveal the dendritic structure and selectively etch the γ' precipitates to aid in quantitatively characterising the microstructure of the alloys. SRR-99 was etched using Marble's Reagent and CMSX-4 and CMSX-10N were both etched using Kalling's No. 2 Reagent. Characterisation of the microstructure was carried out through optical microscopy and in a JEOL JSM-7200 Schottky Field Emission scanning electron microscope (SEM) Energy dispersive X-Ray spectroscopy (EDS) was used to measure and confirm the chemical composition of each alloy using acceleration voltages of 15–20 kV.

2.2. Isothermal oxidation procedure and characterisation

Isothermal oxidation tests were performed on circular test coupons (9 × 3 mm) cut from the cylindrical bars; the top surface of each coupon was prepared finishing with a 1 μm diamond suspension polish. Before testing, the coupons were cleaned in an ultrasonic bath of ethanol for 5 min. The samples were then placed in a preheated electric furnace at 550 °C for individual exposures of 2, 8, 16, 64 and 1000 h, in isothermal lab air conditions. The 1000 h exposure was performed to produce a thicker oxide layer for fuller compositional analyses of the oxide scales forming. One sample was oxidised at each exposure as the focus of this study is on scale formation variation across the range of microstructure exposed

Following oxidation, the samples were examined under SEM to inspect the outer oxide. XRD analysis was performed on the samples oxidised for 1000 h for each of the alloys. Data was collected on a Rigaku SmartLab diffractometer equipped with an in-plane arm, a 9 kW (45 kV, 200 mA) Cu target rotating anode generator and a HyPix 3000 semiconductor detector. A grazing incidence geometry was employed with a fixed grazing angle of 1.0° and a parallel beam configuration. Data were collected from 10 to 90° 2θ using a detector scan and a step size 0.02°. To examine the oxidation sequence, the samples were first nickel plated in a bath of Watt's Solution (at a temperature of 50 °C for roughly 15 min with a potential of 3 V and current of 1.5 A) to preserve the integrity of the external oxide layers, then the coupons were sectioned and mounted in conductive Bakelite and polished to a 1 μm finish in order to inspect the cross-section of the oxide layers under SEM using both secondary electron imaging (SEI) and backscatter electron (BSE) imaging mode.

2.3. Oxide thickness analysis

Both the internal and external oxide layers have been characterised in this study using various techniques. First, the external layer was characterised under SEM through 3D stereoscopic reconstruction using Alicona 3D MeX software. Using stereoscopic imaging, 3D images can be generated of the surfaces from which 3D information and data can be extracted. The software creates a 3D image by combining images of an area of interest taken at 0° tilt (perpendicular to electron beam) and ±5° tilts. Then, once the oxidised coupons had been Ni-plated and sectioned, images of the cross-section were taken under SEM over approximately 0.5 mm length of oxide scale to ensure a statistical representation of the oxide thickness. Only parts of the surface that were sufficiently protected by the nickel plating were imaged and examined. From the BSE images the external and internal layers were initially separated manually using a graphics pen, from this the internal oxide was extracted in ImageJ using a thresholding technique to select and binarise the internal scale thickness (Fig. 1). The binary images of the internal oxides were processed using a MatLab [15] script designed to measure the number of black pixels per column and scale into an average thickness measurement with associated statistical measures (e.g. standard deviation). The resolution of the measurement is dependent on the resolution of the SEM image used in the image analysis, as the measurement counts the number of pixels in the oxide layer. In this study the pixel resolution was 0.005 μm

Table 1

Chemical composition of SX Ni-based superalloys SRR-99, CMSX-4 and CMSX-10N (wt%).

	Al	Cr	Co	Ti	Mo	Ta	W	Re	Hf	C	Ni
SRR-99	5.5	8.5	5.0	2.2	-	2.8	9.5	-	-	0.015	
CMSX-4	5.6	6.5	9.0	1.0	0.6	6.5	6.0	3.0	0.1	-	Bal.
CMSX-10N	5.8	1.6	3.1	0.08	0.45	8.5	5.5	6.8	-	-	Bal.

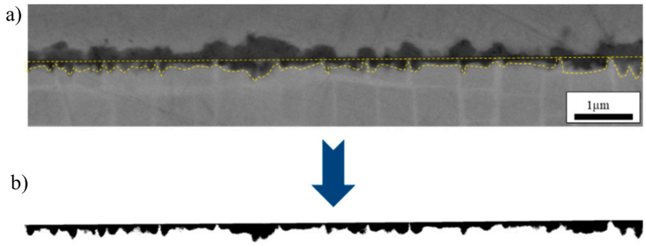

Fig. 1. Method for measuring the internal oxide thickness a) BSE SEM image of the cross-section of the oxidised surface with internal layer highlighted b) the internal layer extracted and image binarised.

2.4. *Thermodynamic modelling*

To assist this study thermodynamic modelling has been used to predict the oxide that could form for each alloy system at 550 °C over a range of oxygen partial pressures. Thermo-Calc 2024.2 software has been used to model the sequence of oxidation in SRR-99, CMSX-4 and CMSX-10N using the TCNI12 database and the CALPHAD approach [16,17]. A more detailed description of Themo-Calc and its applications can be found in reference [18]. For each alloy, the system was defined by entering the composition of the alloy (for SRR-99, C was excluded as it contributes a minor amount to the overall composition so was not expected to affect the results significantly), at a temperature of 550 °C and atmospheric pressure. The variable is defined as the oxygen partial pressure, represented by the chemical activity in Thermo-Calc, ranging from 1×10^{-25} to 1 atm. The chemical composition of individual oxide phases was also calculated in Thermo-Calc.

3. Results

3.1. *Microstructural characterisation*

SEM-BSE images of the polished alloys revealed the dendritic structure of the alloys. Primary dendrite arm spacing for SRR-99, CMSX-4 and CMSX-10N was measured to be 384 ± 25 μm, 596 ± 176 μm and 274 ± 44.8 μm, respectively. Under SEM the γ/γ' structure can be observed for the alloys, Fig. 2. Measurements of the γ' precipitates show an average γ' size of 0.138 μm^2 (±0.03), 0.197 μm^2 (±0.06) and 0.071 μm^2 (±0.01) for SRR-99, CMSX-4 and CMSX-10N respectively. The γ' volume fraction was measured to be 71.8 % (±2.68) for SRR-99, 73.5 % (±2.96) for CMSX-4 and 73.2 % (±2.36) for CMSX-10N. The typical cuboidal γ' structure can be observed in CMSX-4 with a regular and repeating structure. Low magnification SEM images reveal the dendritic structure, the lighter region being the dendrite cores (DC) and the darker being the interdendritic regions (IR) Fig. 2a-c. This brightness contrast is due to the segregation of heavier elements with a higher atomic mass to the DC regions. Due to the addition of carbon to composition of SRR-99, clusters of metallic carbides (MC) are observed within the IRs, highlighted in Fig. 2a. Neither carbides nor porosity were observed in the interdendritic region of CMSX-4, Fig. 2b. For CMSX-10N under higher magnification, patches of γ/γ' eutectic can be found within the IRs, highlighted in Fig. 2c. Clusters of γ/γ' eutectics tend to be found in the IR of single crystal superalloys that have not received a solution heat treatment [19]. The morphology of the γ' precipitates differ between the two regions, being more irregular in the DC and becoming more cuboidal and regular in the IR. Similar observations were made by Park *et al.* [20] in as-cast CMSX-10N having undergone no heat treatments suggesting the CMSX-10N used for this study had not received a fully solutionising heat treatment.

3.2. *Oxide surface morphology*

The development of oxide scale under isothermal conditions at 550 °C from 2 to 1000 h is shown in Fig. 3 for SRR-99, CMSX-4 and CMSX-10N. There are distinct differences in the oxide morphology and oxide distribution between the three alloys. First describing the sequence of oxidation and morphology for SRR-99, after 2 h of exposure the oxide appears more pronounced over the γ' precipitates. This is more pronounced after 8 h where the gaps in the oxide surface, over the γ channels, have been almost completely covered. Beyond 8 h and up the 64 h the morphology of the oxide scale seems uniform and homogeneous across the surface. Additionally, the carbides in SRR-99 have also been found to be readily attacked by oxidation. Fig. 4a shows an example of a carbide that has been oxidised for 2 h at 550 °C; it can be observed that when oxidised the carbide erupts as shown through the 3D image reconstruction (Fig. 4b). In the case of CMSX-4, initial stages of oxidation very clearly reveal the underlying microstructure morphology. There is a clear difference between the oxides forming over the γ channels and the γ' precipitates. The γ channel oxide is interconnected

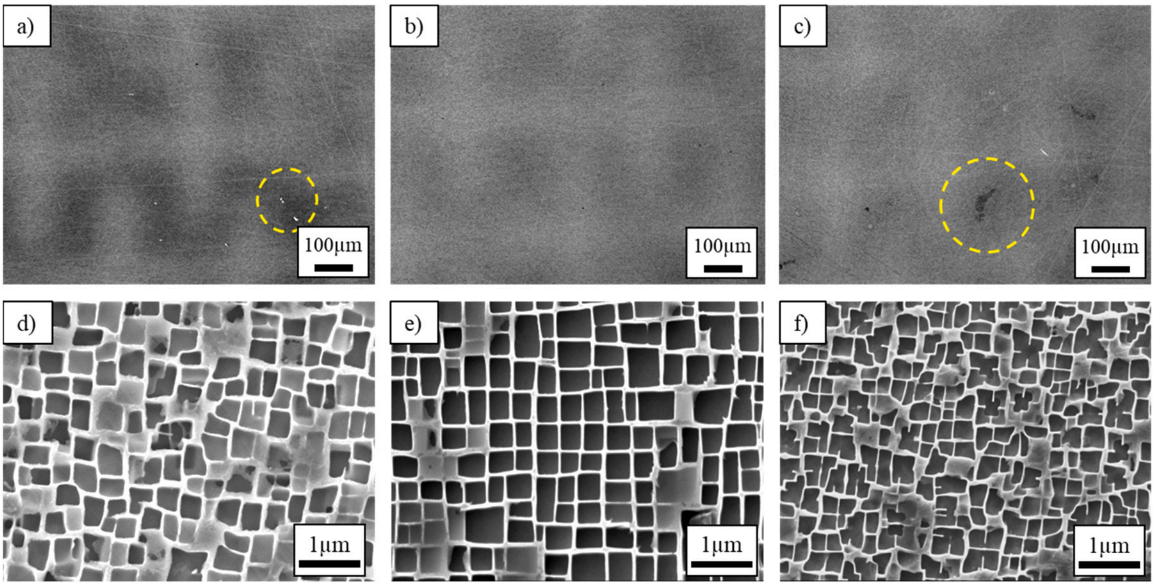

Fig. 2. Low magnification SEM-BSE image of the dendritic structure of a) SRR-99 (carbides circled), b) CMSX-4 and c) CMSX-10N (γ/γ' eutectic circled). High magnification SEM secondary electron images showing the morphology of d) SRR-99, e) CMSX-4, f) CMSX-10N.

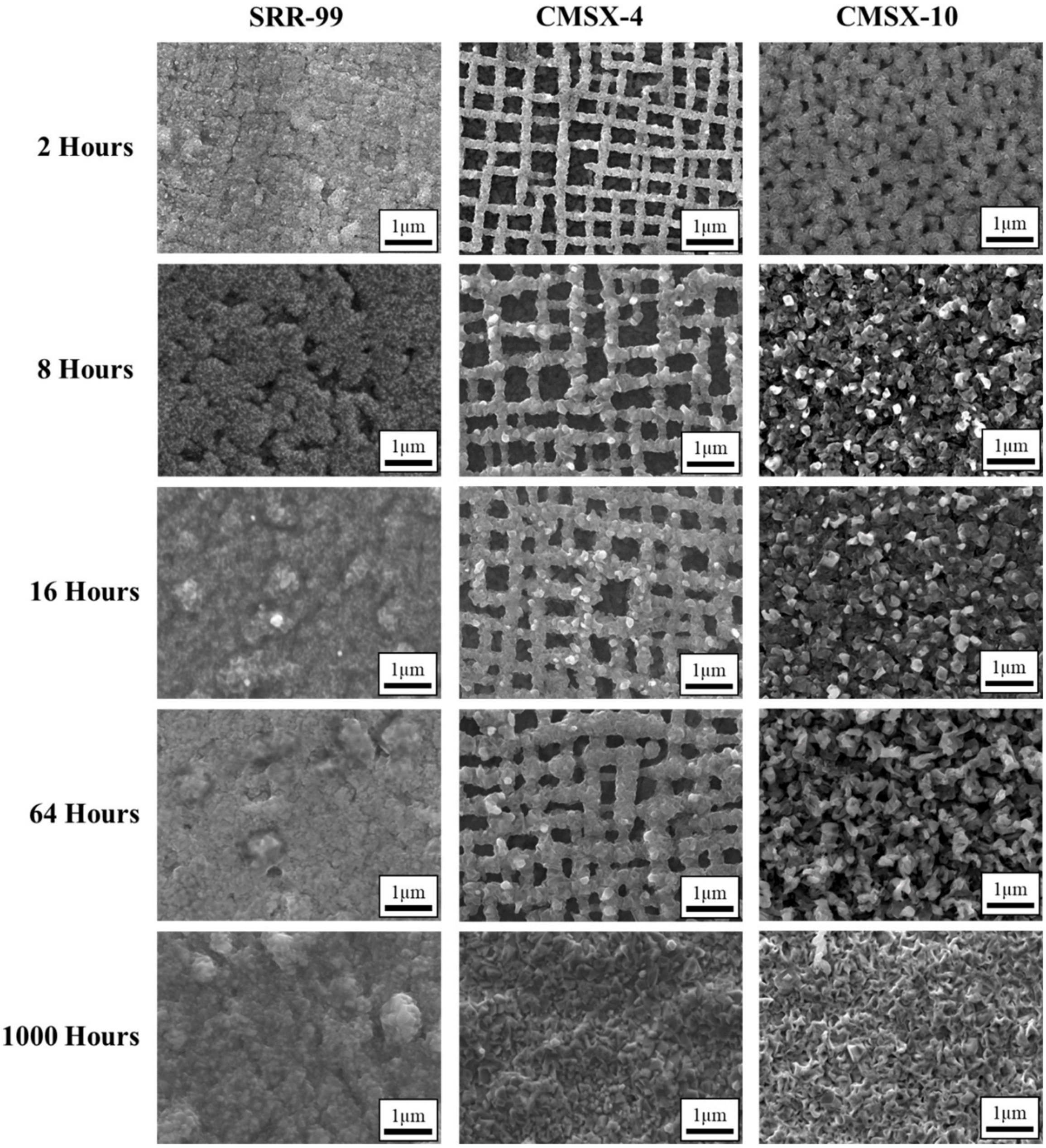

Fig. 3. Secondary electron SEM images showing the oxide scale development on the surface of isothermally oxidised SRR-99, CMSX-4 and CMSX-10N samples at 550 °C.

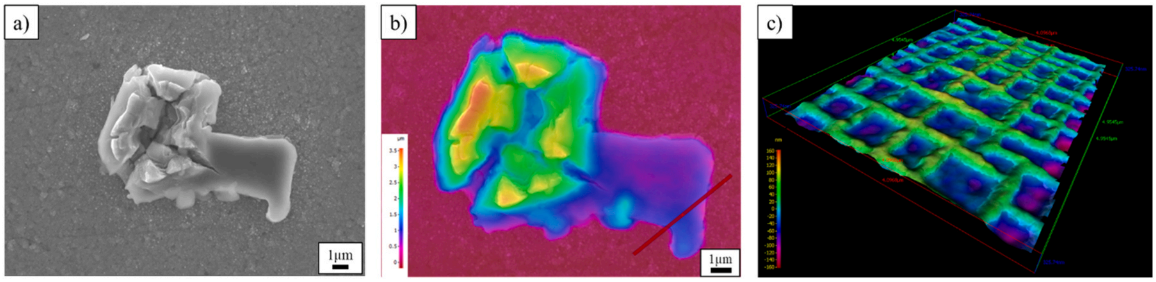

Fig. 4. a) SEM-SEI of an SRR-99 carbide b) 3D reconstruction of carbide eruption c) 3D reconstruction of oxidised CMSX-4 surfaces revealing differences in oxide formations over γ channels and γ' precipitate.

and appears raised from the surface. The oxide scale over the γ' precipitates also appear darker and thinner, as opposed to that observed in the initial stages of oxidation of SRR-99, where oxide over the γ' precipitates appears to be raised. Through 3D imaging reconstruction the raised oxide over the γ channels can be observed in Fig. 4c. As the exposure time increases, the oxide over the γ channels thickens and spreads over the γ’ precipitates. However, even at 64 h exposure, the γ and γ’ microstructure of the alloy is still reflected in the oxide, albeit significantly more obscured. Similar observations of oxide morphology, specifically in early oxidation, have been made in CMSX-4 oxidised at 550 °C [21] and a third generation superalloy at 900 °C [22].

As for CMSX-10N, the oxide morphology appears to be similar to that of CMSX-4 in the initial stages but more severe. After 2 h exposure, oxide build up over the γ channels is still observed with a thinner layer over the γ’ precipitates; however, the oxides over the γ channel have almost completely covered the γ’ precipitates and progressed much further than is seen in CMSX-4 at 64 h exposure. After 8 h exposure, the external oxide scale has become homogenous leading to the underlying microstructure becoming completely obscured. However, the γ/γ’ eutectic phases are still visible, even at the longer exposure times (Fig. 5a). Using 3D imaging reconstruction, a heightmap of the oxide formation over the eutectic regions shows a build-up of oxide around the interface between the γ/γ’ eutectic precipitate and surrounding regular γ/γ’ structure, Fig. 5b. The oxide height then plateaus further away from the interface as the oxide becomes homogenous, as shown by the height profile measurement in Fig. 5c for CMSX-10N after 64 h exposure.

After 1000 h exposure at 550 °C, the external oxide morphologies for all the alloys now appear homogenous with no outline of the underlying microstructure visible on the oxidised surface of CMSX-4 either at this stage. A slight waviness on the oxide is also observed on the surface morphology of CMSX-4.

3.3. Oxide cross-section

The development of the external and internal oxides for SRR-99, CMSX-4 and CMSX-10N is shown in Fig. 6. The single crystal substrate is identifiable by the γ/γ’ microstructure revealed by the BSE SEM mode; the oxide layer has a dark contrast and is seen to protrude above the surface and penetrate the substrate. Above the oxide layer the nickel-plated layer can be seen, in some instances the plating can be seen to have detached with the external oxide layer. It is clear from Fig. 6, the progression of the oxide growth is more severe for CMSX-10N, with the internal oxidation penetrating deeper into the substrate than both SRR-99 and CMSX-4. It is worth noting that the adhesion of the nickel plating was worse for CMSX-10N, leading to consistent measurements of the external oxide from the cross-section of the sample not being able to be taken. This suggests that the adhesion of the external oxide layer for CMSX-10N is weaker than that of the other two alloys. Isothermal oxidation studies of CMSX-10N performed by Akhtar *et al.* [23] at 800, 900 and 1000 °C also found that there was poor external oxide adhesion to the substrate, only becoming well bonded at 1000 °C. Initial stages of oxidation after 2 h, Fig. 6a, show a non-uniform layer of external oxides forming predominantly over the γ channel for both CMSX-4 and CMSX-10N. This is supported by the observations made on the external oxide in Fig. 3. However, as the oxidation reaction continues with longer exposure durations, Fig. 6b, it is observed that an internal oxide layer forms preferentially attacking the γ’ precipitates. This is especially apparent in CMSX-10N where the internal oxidation penetrates multiple rows of γ’ precipitates below the surface. In the case of SRR-99, further oxidation shows preferential oxidation along the γ channels instead of the γ’ precipitates.

Fig. 7 highlights the path of oxidation for CMSX-4 and SRR-99 after 64 h exposure. In CMSX-4 the oxidation path is along the γ/γ’ interface whilst also preferentially oxidising the γ’ precipitates leaving fingers of the γ phase reaching to the surface. This observation supports the mechanism proposed by Evangelou *et al.* [21] by which oxygen diffuses down the γ/γ’ interfaces due to the higher localised stress states on the interfaces caused by the different lattice parameters of γ and γ’. A similar mechanism could explain the behaviour seen in SRR-99, with preferential oxidation occurring along the γ/γ’ interface, but instead preferentially oxidising the γ phase rather than the γ’ phase, this difference in behaviour will be discussed later.

The internal oxide thickness has been measured using transverse sections of the coupons. The external oxide was not measured in this way as it was found that the nickel plating had poor adhesion to some of the test coupons; therefore, in some instances the external oxide was lost or damaged during the sectioning and sample preparation stage. Thus, focussing on internal oxide thickness measurements was considered as a more systematic approach as an evaluation to compare the oxidation kinetics. Instead, the external oxide has been characterised through profile measurements taken from 3D image reconstruction, as shown in Fig. 4 and Fig. 5. In the case of CMSX-4 the measurements are taken across the γ channel to show the difference in external oxide thickness between the scale over the γ’ precipitate and γ channel; therefore, these measurements are taken as a relative height and not as a true measure of the external oxide thickness. Similar measurements were taken for CMSX-10N; however, due to the rapid growth of oxide obscuring the underlying microstructure, the profile measurement was taken at eutectic phases with one taken at the interface and another far field measurement compared to the oxide over the γ/γ’ eutectic.

The oxide scale thickness results compared to exposure duration for each of the alloys are shown in Fig. 8. Through assessment of the relative external oxide thickness difference over the γ’ compared to the γ channel the results are shown in Fig. 8a. For CMSX-4 the difference between oxide height over the γ and γ’ phases remain relatively constant suggesting that once an initial build-up of oxide over the γ channel has formed, at a short duration (not captured in this study) the growth of oxide over the γ’ and γ are similar. However, for CMSX-10N, external oxide which has formed over the γ channels continues to grow at a faster rate than the oxide over the γ/γ’ eutectic and is even more severe at the

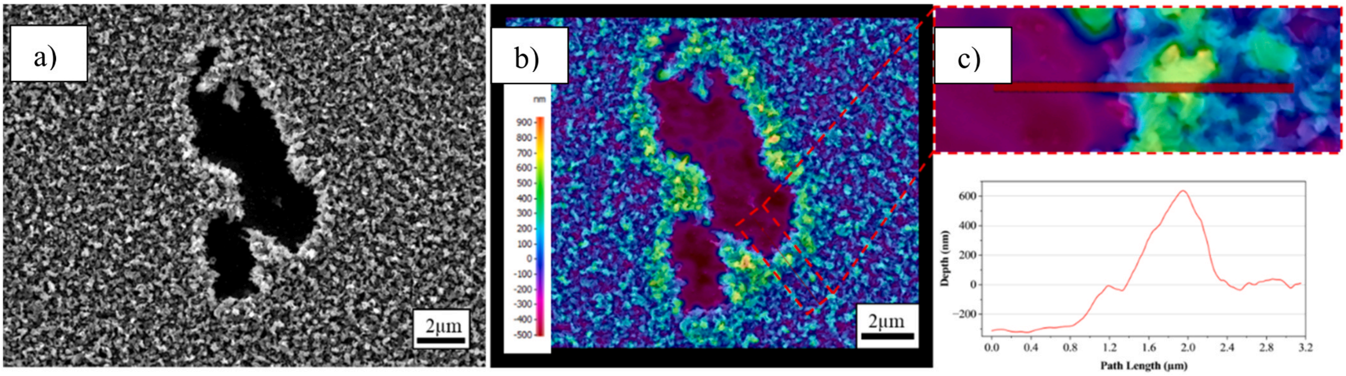

Fig. 5. a) SEM image showing a γ/γ’ eutectic on the oxidised surface of CMSX-10N after 64 h at 550 °C, b) 3D reconstruction of oxidised eutectic, c) height profile scan taken along the eutectic interface.

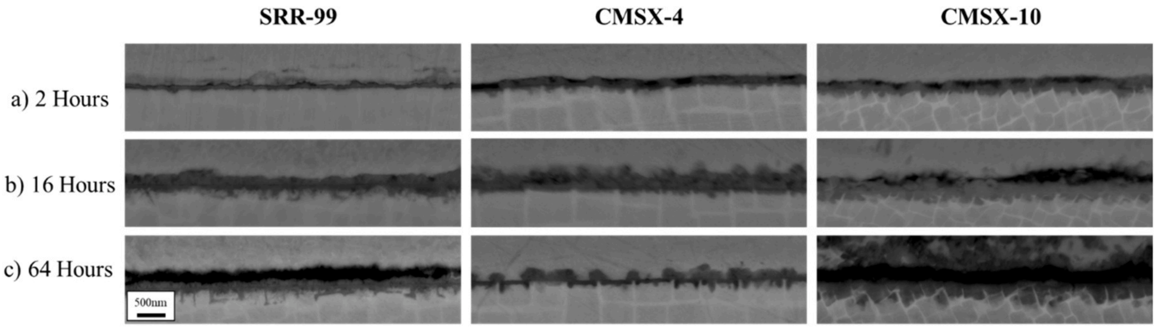

Fig. 6. BSE images of the oxide profile development on the surface of SRR-99, CMSX-4 and CMSX-10N isothermally oxidised at 550 °C.

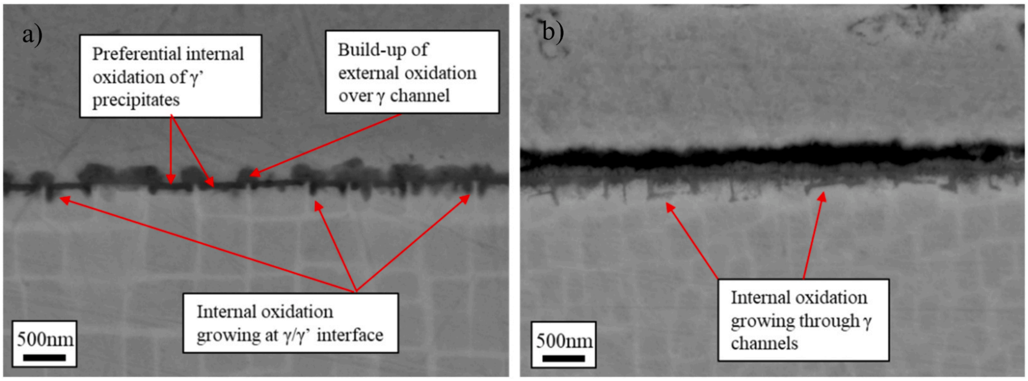

Fig. 7. BSE images of a) CMSX-4 and b) SRR-99 oxidised at 550 °C for 64 h showing the profile of the internal and external oxides.

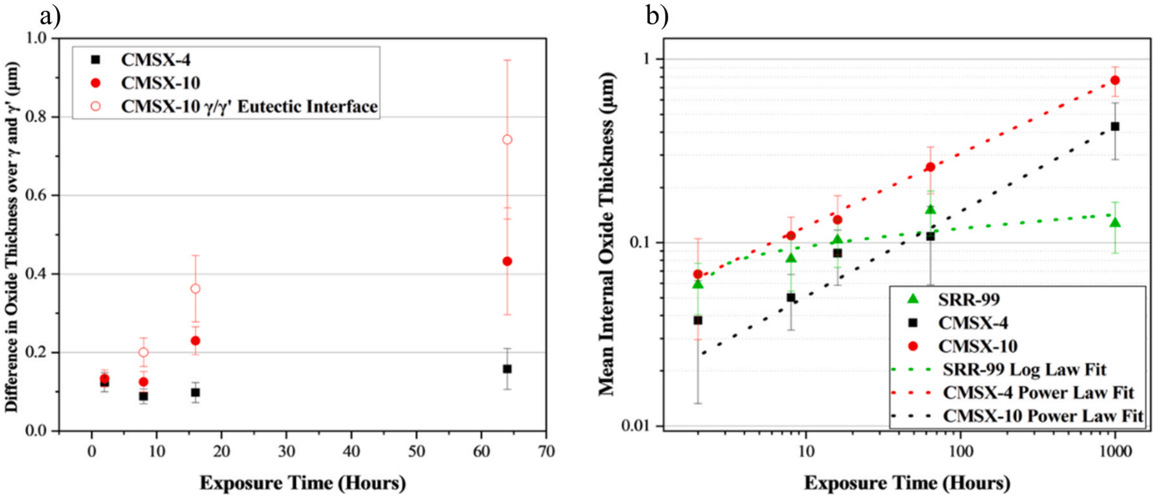

Fig. 8. a) External oxidation thickness measured through 3D imaging reconstruction b) oxidation kinetics of SRR-99, CMSX-4 and CMSX-10N at 550 °C as a function of internal scale thickness.

interface. The internal oxide thickness measurements up to an exposure of 1000 h are shown in Fig. 8b on a log-log plot. For each alloy a fit has been applied to show which law the oxidation kinetics follows. This is discussed further in the Section 4.1. Up to 64 h, as expected, the internal oxide thickness is seen to increase with longer exposure times for each alloy. The oxide thickness of CMSX-10N is the greatest out of the three alloys; the oxide has grown the least in CMSX-4, and somewhat surprisingly, SRR-99 lies in between CMSX-10N and CMSX-4. However, advancing to an exposure of 1000 h reveals the oxide thickness of SRR-99 has plateaued whereas the oxide of CMSX-4 has continued to grow, as is also seen in the CMSX-10N study.

3.4. Oxide composition characterisation

The results from the XRD analysis are shown in Fig. 9. Scans of each alloy revealed strong peaks associated with the formation of NiO, which is to be expected. In SRR-99 transition alumina were found to be present: the low angle peaks at roughly 19° and 27° correspond to γ-Al_2O_3 and η-Al_2O_3 respectively [24,25]. As for CMSX-4 and CMSX-10N, XRD detected the spinel Co_3O_4, although the peaks in CMSX-10N are very small suggesting the majority of the oxide is comprised of NiO.

To determine the chemical composition of the internal and external oxides formed during oxidation at 550 °C, EDS line scans were taken across the oxide scale layers (including both internal and external

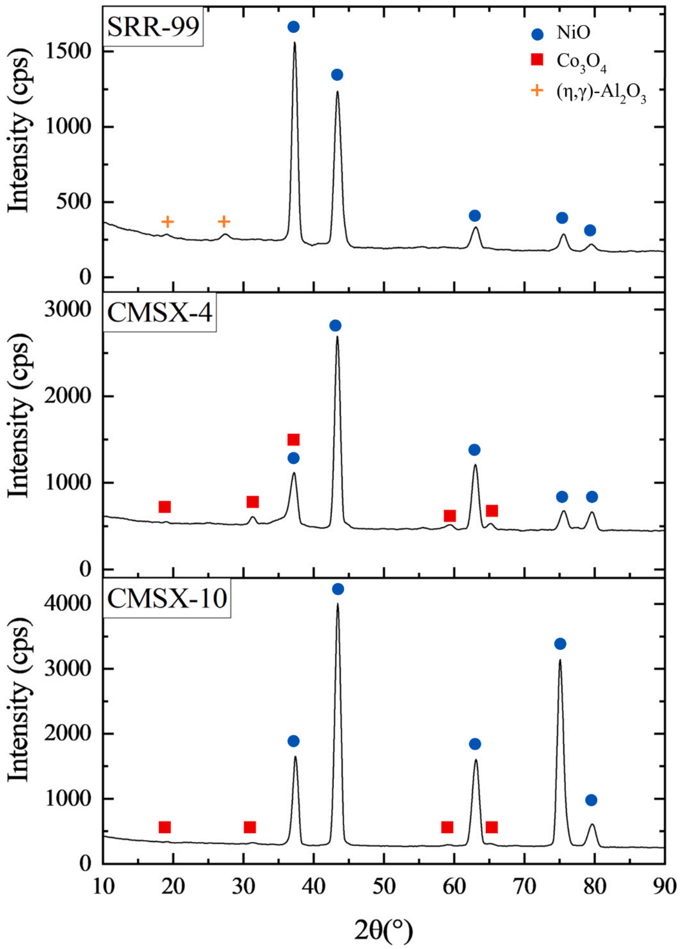

Fig. 9. XRD diffraction pattern of SRR-99, CMSX-4 and CMSX-10N oxidised at 550 °C for 1000 h.

oxides) on samples exposed for 1000 h. The results of the EDS line scan analysis are shown in Fig. 10; the separation between the internal and external oxides have been shown by the black dashed lines. The line scans for SRR-99 and CMSX-10N also cross the Ni-plating, which was applied to protect the integrity of the oxide scale, and this can be seen on the line scan data where only Ni (and Co) are detected over the external oxide. For SRR-99, CMSX-4 and CMSX-10N the external oxide is predominantly Ni based but also with a detectable level of Co. Internally, where O is detected, there is an increase in Al aligned with a decrease in Ni for each of the alloys; furthermore, in CMSX-4 and CMSX-10N, an increase in W, Ta and Re is detected in the internal oxide region alongside Al. There is not a detectable increase in W or Ta in the internal oxide layer for SRR-99. Additionally, in SRR-99 and CMSX-4 a slight increase in Ti has been detected in the internal oxide layer but not for CMSX-10N. Furthermore, from the cross-section of the 1000 h CMSX-4, both the internal and external oxide layers appear to be uneven and wavy; a similar observation was made in the previous section when observing the surface morphology of the 1000 h oxidised sample. From the cross-sectional view, where the internal oxide has penetrated deep into the substrate, the external oxide is also thicker, showing that more Ni has migrated to the surface and oxidised in these regions. It is important to note that the scans for SRR-99 and CMSX-4 are significantly shorter than that of CMSX-10N as the oxide layers are much thinner; therefore, the EDS scans are going to be affected more heavily by the underlying microstructure and may not fully represent oxides formed. This is evident in the scan for SRR-99 as there appears to be two peaks for Cr which both correspond to the γ channels, and does not necessarily indicate a Cr-rich oxide has been formed.

4. Discussion

4.1. Oxidation kinetics

To better understand the oxidation kinetics behaviour of each alloy, an attempt to fit generic power law (Eq. 1) [26], was made on the measurements of the internal oxide thickness,

$$x^n = k_r t \tag{1}$$

where x is the oxide thickness, k_r is the reaction constant, and n is a constant. Additionally, a logarithmic law (Eq. 2) [9,27] was also fitted to the data,

$$x = k_{\log}\log(t + t_0) + A \tag{2}$$

where x is the oxide thickness, k_{log} is the logarithmic reaction constant, and t_0 and A are constants. For the fitting process, weights were assigned to each data point to account for the variance in the data using weight $= 1/\sigma^2$, where σ^2 is the variance (calculated from the standard deviation indicated by the error bars in Fig. 8b). The coefficient of determination, R^2, value has been calculated and shown to indicate how good the law fit is for the data. This approach has been used to determine the growth law which most accurately describes the data [28]. The values of the fitting parameters for the power law are shown in Table 2 and for the logarithmic law are shown in Table 3. In the case of the power law, a value of n near to 2 would indicate the oxidation kinetics follows a parabolic law.

It has been well documented that the isothermal oxidation growth rate of Ni-based superalloys follows a parabolic law [29–32], suggesting that the rate controlling factor is the diffusion of ions through the oxide scale as described by the Wagner theory [9,33]. Other laws have been derived for the oxidation of metallic materials such as the linear law, which is generally used to describe the oxidation of light metals that can burn in air such magnesium [34]; or the logarithmic law, which has been used to describe the initial formation of thin film oxides at intermediate temperatures [35,36]. For this reason, both a generic power law (if $n = 2$ in Eq. 1 then the fit is parabolic) and a logarithmic fit were attempted in Fig. 8b. Both CMSX-4 and CMSX-10N behaved similarly and showed near parabolic behaviour, whereas neither the power nor logarithmic fit provided a good description for the behaviour seen in SRR-99. However, these results only describe the partial kinetics of the alloys as only measurements from the internal oxide layer were used.

The effect of γ' size and distribution must also be considered in the oxidation kinetics of the alloy. A study into the effect of γ' size on the oxidation resistance of polycrystalline IN738LC between 750 and 950 °C reported a decrease in oxidation resistance for alloys with a smaller γ' size [37]. This has been attributed to the faster depletion of smaller γ' due to preferential oxidation of Al, quickly creating a precipitate free zone exposing the γ matrix to oxidation. The larger precipitate size was found to decrease the internal oxidation rate. In our current study, up to 64 h exposure at 550 °C a similar trend has been observed, as the alloy with the smallest measured γ' size, CMSX-10N, appears to be the least oxidation resistant and the alloy with largest measured γ' size, CMSX-4, shows the slowest kinetics. Although, the precipitate sizes compared in [37] were 800 nm and 50 nm, a much larger size disparity than was measured in alloys tested in this study, suggesting the effect of γ' size on difference in oxidation behaviour may be minor compared to other factors. Additionally, there is opposing literature on the effect of γ' size on oxidation resistance. An investigation into the effect of γ' size in single crystal superalloy at 650 °C found poorer oxidation resistance in the alloy with larger precipitate size [38]. It was proposed that this behaviour was caused by large laterally growing Ni-Al spinel promoting inward and outward diffusion of ions assisting in oxidation in the alloy with large γ' size, but for the alloy with a smaller γ' size a continuous protective alumina layer was formed, slowing the oxidation kinetics.

Aluminium and chromium are well known to play a vital role in the oxidation resistance of Ni-based superalloys through formation of stable

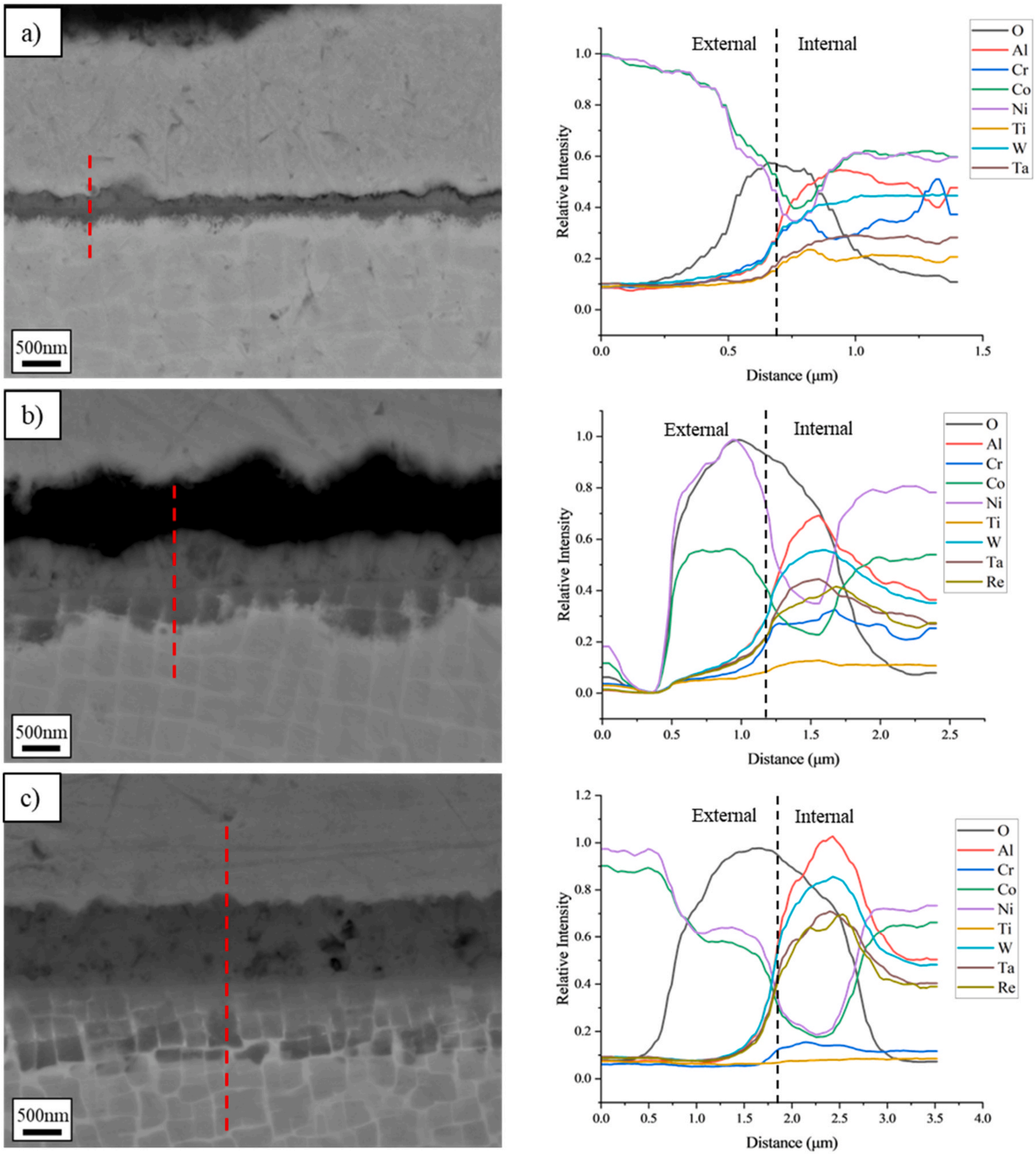

Fig. 10. BSE images showing the cross-section profile of the internal and external oxide scale after 1000 h for a) SRR-99, b) CMSX-4 and c) CMSX-10N. To the right of each image is an EDS line scan for that alloy in the region shown by the red dashed line.

Table 2
Oxidation power law rate constants for the internal oxides formed on CMSX-4 and CMSX-10N when oxidised isothermally at 550 °C.

Alloy	k_r ($\mu m^n/h$)	n	R^2
SRR-99	1.61×10^{-10}	8.19	0.674
CMSX-4	1.16×10^{-4}	2.40	0.933
CMSX-10N	5.20×10^{-4}	2.47	0.997

Table 3
Oxidation logarithmic law rate constants for the internal oxidation SRR-99, CMSX-4 and CMSX-10N when isothermally oxidised at 550 °C.

Alloy	k_{log}	A	t_O	R^2
SRR-99	0.0098	0.0746	−1.80	0.829
CMSX-4	0.141	−0.564	77.0	0.920
CMSX-10N	0.214	−0.747	41.8	0.996

and adherent oxides preventing further oxygen diffusion into the substrate, therefore, these elements are highly influential in the kinetics of oxidation. Concerns have been raised about the decrease in these protective oxide-forming elements, especially Cr, in later generation superalloys and the effects this may have on the performance of turbine blades in high temperature environments [23]. In an investigation of the oxidation kinetics at 550 °C of two SX superalloys with different levels of Cr at 550 °C, CMSX-4 and MD-2 with Cr content of 7.53 at% (6.41 wt%) and 9.39 at% (8.08 wt%) respectively, CMSX-4 was found to have faster oxidation kinetics with thicker oxides forming, suggesting that the reduced level of Cr reduces the effectiveness of the oxides to prevent the diffusion of oxygen to the substrate [21].

Similarly, the kinetics of SRR-99, CMSX-4 and RR3000 (also referred to as CMSX-10K [39]) has been investigated through thermogravimetric analysis (TGA) at 800, 900 and 1000 °C up to 100 h exposure [40]. As with this current study, SRR-99 possesses the highest Cr content with RR3000 containing the least. It was found that for each temperature, CMSX-4 possessed the slowest oxidation kinetics, with RR3000 having the fastest at a magnitude faster than both CMSX-4 and SRR-99. At 1000 °C both RR3000 and SRR-99 experienced mass loss over time, resulting in RR3000 plateauing after 30 h and SRR-99 losing mass at a linear rate for the last 80 h. This shows that even though SRR-99 contained more Cr that CMSX-4, this does not necessarily equate to better oxidation resistance, at least up to 100 h exposure. At 550 °C, a similar result has now been observed up to 64 h exposure through measurement of the internal oxide thickness (Fig. 8b), showing the oxide has grown the least in CMSX-4 and most in CMSX-10N with SRR-99 in between. It is again worth emphasising that the oxide kinetics derived in this work only consider the internal oxide, however TGA includes both the internal and external oxide growths, but TGA is beyond the scope of this study.

4.2. Thermodynamic simulations

The oxidation kinetics and sequence of oxide formation is reliant on the thermodynamics of the oxide species in the metal system. Depending on the temperature and oxygen partial pressure of a system, thermodynamic calculations can predict which stable oxide species will form. The plots calculated by Thermo-Calc, Fig. 11, show the stable oxide phases formed in each of the alloy systems at 550 °C as a function of the oxygen partial pressure. For SRR-99, CMSX-4 and CMSX-10N (Fig. 11a-c), in the high oxygen partial pressures regions the dominant phase is halite in the form of NiO. This is consistent with experimental observations as NiO is observed as an external oxide layer where the oxygen partial pressure is highest. Going down to a pressure of 10^{-21} the formation of NiO abruptly stops, below which the formation of disordered FCC $L1_2$ is found. The FCC $L1_2$ phase predicted is disordered as Al in the system has been used in the other oxides predicted at these partial pressures. This transition point can be seen at the surface of the alloys where higher partial pressures above the transition represents external oxide scales attached to the surface of the metal, and oxides forming at lower partial pressure represent the internal oxides formed subsurface. For CMSX-4 and CMSX-10N (Fig. 11b-c), due to the similar composition of the alloys, Thermo-Calc has predicted they share mostly the same oxides; however, there are significant differences in the volume fractions of certain oxide species formed between the alloys, such as the spinel phase that has formed at high partial pressure, which is significantly higher in CMSX-4 or the volume fraction of corundum formed at low partial pressure that is almost double in CMSX-10N.

The other significant oxide products calculated are spinel oxides, and in SRR-99 and CMSX-10N two different spinel oxide species have been predicted. The spinel Al_2NiO_4 was calculated in both SRR-99 and CMSX-10N, this is a common spinel formed externally. However, this spinel has not been calculated in the CMSX-4 model. Fig. 12 shows the calculated composition of the second spinel predicted in SRR-99 (Fig. 12a) and CMSX-10N (Fig. 12b), it was also calculated that the only spinel predicted for CMSX-4 shared the same composition as the spinel formed for CMSX-10N (Fig. 12b). For SRR-99, these results indicated that the predominant element (other than O) in this spinel is Cr. However, in the case of CMSX-4 and CMSX-10N, Al is the main component of the spinel at high partial pressures but then switches to Cr at lower partial pressures.

It is important to consider some of the limitations associated with this method of predicting oxide phases. That the results obtained from the simulations predict the oxides formed at equilibrium and the simulations do not consider the kinetics of oxide species and how they change as oxides grow. Experimentally an equilibrium state may require far longer to achieve than has been tested in this study; therefore, some of the phases predicted here may not have been able to form even after 1000 h exposure. Additionally, this model has not considered the kinetics of ion transport though the oxide species formed, and the change of kinetics as different oxide phases and scales grow, inhibiting diffusion of ions. Hence, the oxides predicted by Thermo-Calc, especially at very

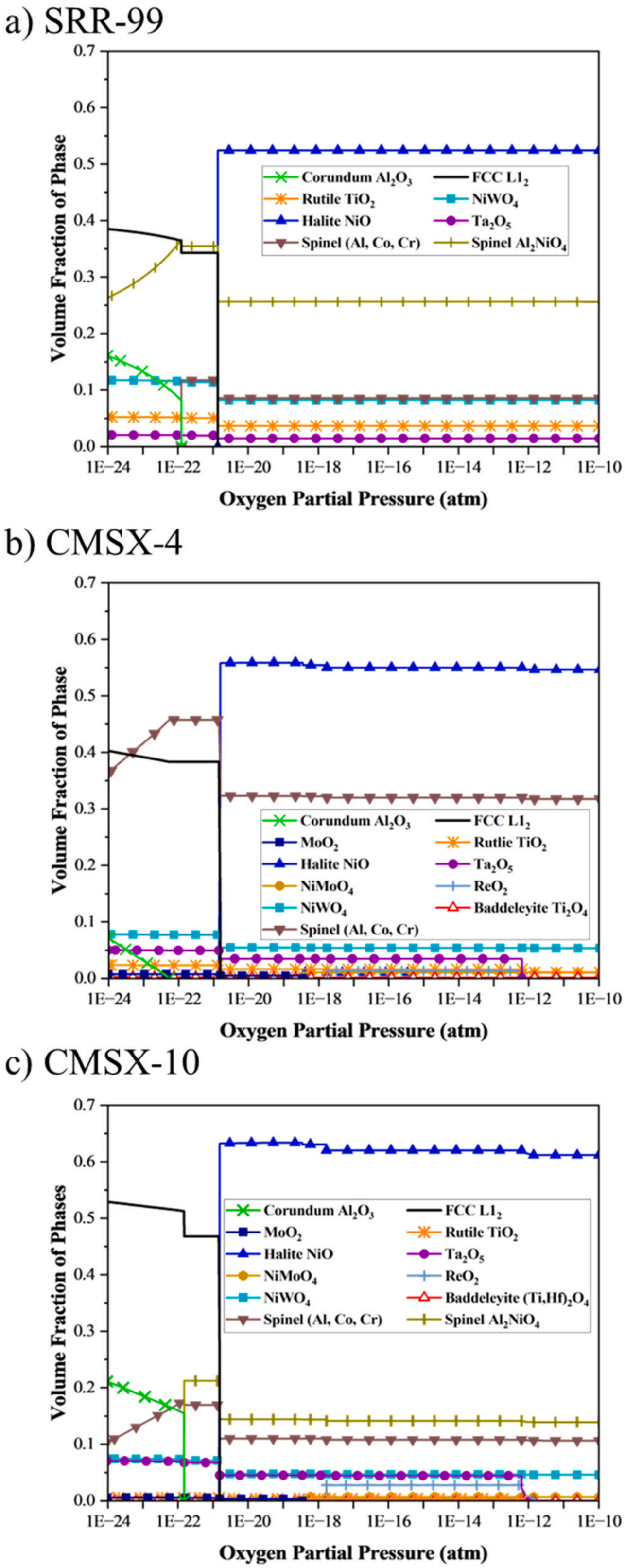

Fig. 11. Thermo-Calc simulations of the stable oxide phases formed on a) SRR-99, b) CMSX-4, c) CMSX-10N at 550 °C.

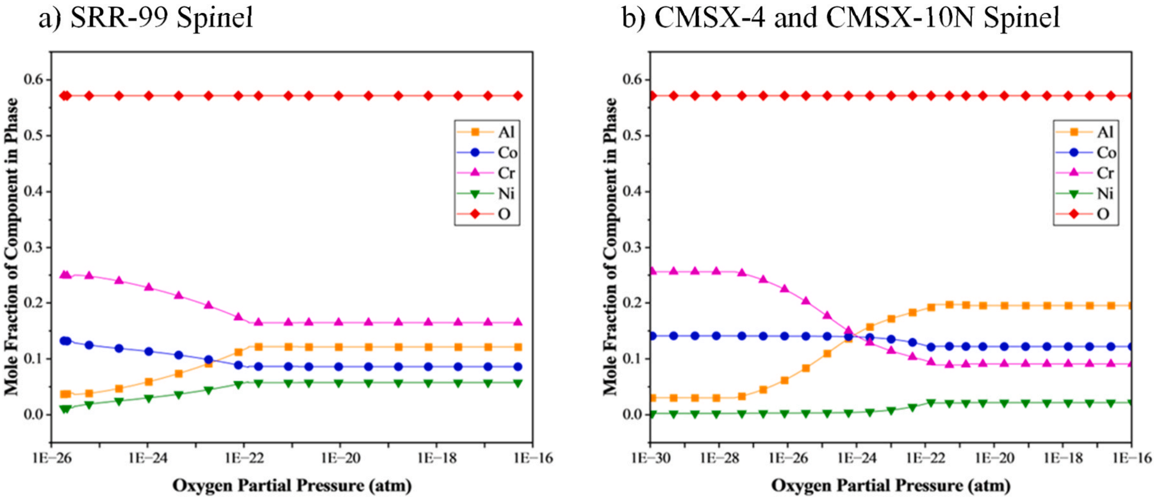

Fig. 12. Calculated composition of the spinel phases in a) SRR-99 and b) CMSX-4 and CMSX-10N.

low oxygen partial pressures, may not be able to form experimentally or even in service due to the oxidation kinetics [17]. Finally, the results are dependent on the database used, TCNI12 data was the latest and most complete database available for use in this study. This database does not contain the relevant information of transition aluminas, so these species will not be predicted in the calculations even though they have been detected through XRD analysis of SRR-99.

XRD and EDS analysis are generally in agreement with most of the phases predicted, especially the order in which they form due to oxygen partial pressure. The calculations did predict α-Al_2O_3, corundum, which is a desirable and protective oxide in Ni-based superalloys. However, XRD results have shown transition alumina in SRR-99, Fig. 9a. Although α-Al_2O_3, is the most stable and desirable form of alumina due to its protective nature in Ni-base superalloys, there exists a host of transition phases of alumina that are not considered stable and are formed in a sequence of reactions that leads to the formation of the stable α phase [41,42]. The sequence and types of transition alumina species formed depends on the temperature and composition [43,44]. Transition γ-Al_2O_3 and η-Al_2O_3 have been described as low temperature alumina phases reported to form at 600 °C [45]. It is interesting therefore, that the transition aluminas have only appeared in SRR-99, but this could help describe the change in kinetics of SRR-99. The oxidation kinetics of SRR-99 initially is faster than that of CMSX-4, but moving to the 1000 h exposure signs of alumina forming have been found in SRR-99 and not CMSX-4, which now has a thicker layer of oxide than SRR-99 at 1000 h.

4.3. Oxidation mechanism

It is clear that the oxidation mechanism and rate are greatly affected by the composition of the alloy, and this has been shown through the observations and simulations of this study. Based upon this work, the following mechanism of oxidation is proposed for CMSX-4 and CMSX-10N. Assuming a clean flat surface, initial oxidation begins with the formation of a thin NiO film with Ni cationic diffusion upward towards the surface of the alloy. A recent study has shown that initial oxidation starts and progresses along the γ/γ' interface [22]. Although the ordered γ' precipitates are coherent with the disordered γ phase, there is still a slight difference in the lattice parameters of the two phases leading to a negative lattice mismatch, δ, causing a stress in this region. The value of δ is dependent on temperature and composition of the alloy, with an increase in temperature resulting in a more negative value of δ. Re has also been shown to have a strong influence on δ as it partitions solely to the γ phase, increasing the lattice parameter making the lattice misfit more negative [46].

For this study the three generations of superalloys contain different levels of Re, as shown in Table 1, so it can be assumed that SRR-99 will have the least negative δ, as it contains no Re, with δ becoming more negative in CMSX-4 and the most negative δ in CMSX-10N with 6 wt% Re. This is supported by a study investigating and modelling lattice misfit in single crystal superalloys at −170 °C, that calculated $\delta = -2.4 \times 10^{-3}$ in CMSX-4 and $\delta = -1.5 \times 10^{-3}$ in SRR-99 [47]. Additionally, at −170 °C, as-cast CMSX-10 has been shown to possess a more negative δ (-5.7×10^{-3}) than CMSX-10 after a standard heat treatment (-2.7×10^{-3}) [48]. This further suggests that the CMSX-10N used in this study will have the most negative δ, not only due to high Re content, but also due to insufficient heat treatment as shown through the microstructure. The stress at the interface induces faster diffusion of Ni ions outward towards the surface, where preferential outward diffusion of Ni to the interface can explain the reason for bulges of NiO forming over the γ channels. This is especially apparent around the coarse eutectic phases of CMSX-10N, as the incoherent γ/γ' interface around the eutectic phase allows for the easy diffusion of Ni, creating the distinctive oxide ridge at the interface as seen in Fig. 5. Where the γ' is exposed on the surface, a thin layer of Al-rich oxide is formed, where Ni and O diffusion through the scale is slower than through the porous NiO oxide over the channels [21,49], so at longer exposures, the oxide growth over the precipitates is slower than over the channels. In the case of both CMSX-4 and CMSX-10N, Ni ions initially migrate from the γ' precipitates at the interface, illustrated in Fig. 13a, and this process leaves vacancies in the γ' lattice structure [22]. The outward diffusion of Ni ions in the γ' precipitate, allows for inward diffusion of O ions down the γ/γ' interface, Fig. 13b, and the internal oxidation of the Al within the γ' precipitates [22,50]. This process is also accelerated by the negative δ, which is also increased in magnitude at higher temperatures [2,46]. This is shown to be due to the thermal expansion of the γ phase being higher than that of the γ' [51], creating an additional tensile strain on the γ' precipitate, promoting stress assisted oxidation in the γ'. The preferential internal oxidation of γ' has also been attributed to Al having a higher affinity to oxygen than other alloying elements, hence γ' oxidise preferentially due to the high Al content compared to the γ matrix [52]. However, this alone cannot explain the difference in oxidation kinetics seen between the two alloys. The δ value can explain why the preferential oxidation of the γ' precipitates is far more severe in CMSX-10N than CMSX-4, as the larger negative δ value, assumed through the higher Re content as well as the apparent insufficient heat treatment of CMSX-10N, will induce a higher stress in the γ' causing more advanced oxidation for a given exposure as observed in Fig. 6. Internally, the decreased oxygen partial pressure thermodynamically favours the oxidation of Al over Ni, as predicted by the Thermo-Calc simulations.

However, this type of mechanism is not observed in SRR-99. Instead

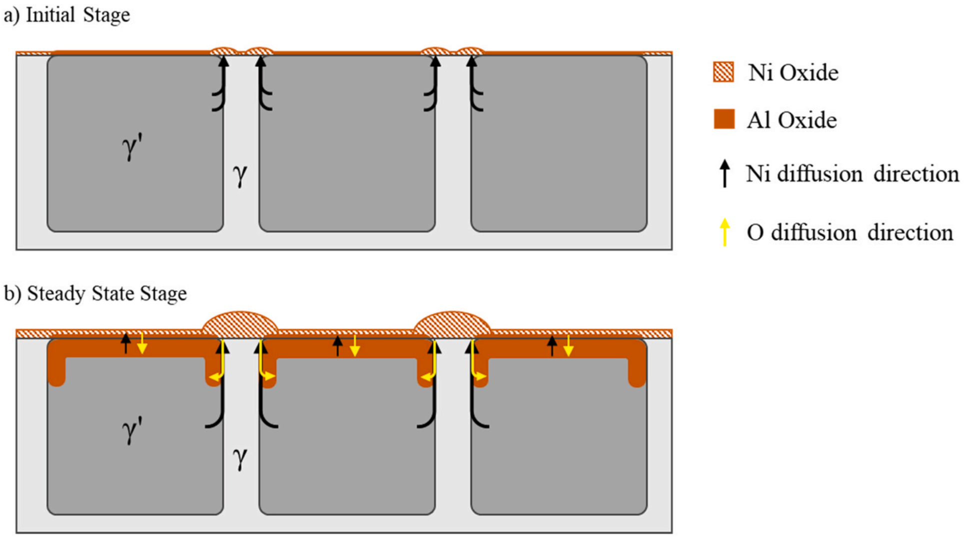

Fig. 13. Schematic showing the early sequence of isothermal oxidation of CMSX-4 and CMSX-10N at 550 °C.

of the γ’ being preferentially oxidised internally along the γ/γ’ interface it is the γ channels that are being attacked and oxidised. Further understanding and investigation into the role of lattice misfit at the γ/γ’ interface at 550 °C is required to help describe the sequence and mechanism of oxidation in SRR99.

5. Conclusions

In this study, the oxidation behaviour of three generations of single crystal superalloys at 550 °C has been investigated. Isothermal oxidation tests have been performed with the aim of assessing the effects of compositional changes between different generations of superalloys on the oxidation kinetics, oxide species formed and oxidation mechanisms. The following conclusions can be drawn:

1. Microstructural characterisation has been performed across each of the three alloys. For both SRR-99 and CMSX-4, the expected γ’ morphology was seen with γ’ volume fractions consistent with alloying composition. Carbides were also found residing in the interdendritic regions of SRR-99. Through observation of the γ’ morphology and identification of γ/γ’ eutectic phases in CMSX-10N, it was determined that the CMSX-10N material used in this study had not received a full solution heat treatment.
2. Examination of the oxidised surface and cross-section of the oxide layers in each alloy at different exposure durations revealed the sequence of oxidation. CMSX-4 and CMSX-10N behaved similarly, with the external oxide scale preferentially building up over the γ channels and eventually covering the underlying microstructure to leave a homogenous external scale; internally, the γ’ precipitates were preferentially oxidised with CMSX-4 showing oxidation initially attacking the γ/γ’ interface. However, for SRR-99 the surface oxide morphology initially built up over the γ’ and internally the γ channels seemed to be oxidised preferentially.
3. The oxidation kinetics at 550 °C under isothermal conditions has been characterised through measurements of the internal oxide layer over a range of exposure times. Interestingly, up to 64 h exposure CMSX-4 showed the slowest oxide growth; however, at 1000 h the thinnest oxide layer was measured in SRR-99. The isothermal oxidation behaviour of CMSX-4 and CMSX-10N obey a near-parabolic law at 550 °C. A logarithmic law is more suitable for describing the isothermal oxidation behaviour of SRR-99 at 550 °C.
4. Through thermodynamic calculation, a complex series of oxides have been predicted to have formed in each of the alloys. Due to their similar chemical compositions, the predicted oxides for CMSX-4 and CMSX-10N are similar, XRD and EDS support these results showing the majority of the oxides formed are NiO and Co_3O_4, found in the external oxide. The transition alumina, (η, γ)-Al_2O_3, was detected in SRR-99.
5. An oxidation mechanism for CMSX-4 and CMSX-10N has been proposed as follows. Assuming a clean flat surface, oxygen initially reacts with the Ni over the γ channels and Al over the γ’ precipitates forming a thin external scale. At the same time, Ni diffuses out of the γ’ phases and up the γ/γ’ interface, oxidising at the surfaces causing bulges of NiO at the interface at the surface and eventually bulges covering the entire γ channel. Due to the non-protective and porous nature of NiO, oxygen is able to diffuse through the external scale and preferentially travel down the γ/γ’ interface and oxidises the Al rich γ’ precipitate, which is thermodynamically favourable at the lower oxygen partial pressure.

Data Statement

All data supporting this study are openly available from the University of Southampton.

CRediT authorship contribution statement

Joseph C. Doyle: Writing – original draft, Visualization, Validation, Methodology, Investigation, Formal analysis, Data curation. **Edward A. Saunders:** Writing – review & editing, Supervision, Resources. **Jane M. Woolrich:** Writing – review & editing, Supervision, Resources. **Mark E. Light:** Writing – review & editing, Formal analysis. **Nong Gao:** Writing – review & editing, Supervision. **Philippa A.S. Reed:** Writing – review & editing, Supervision, Project administration, Conceptualization.

Declaration of Competing Interest

The authors declare that they have no known competing financial interests or personal relationships that could have appeared to influence the work reported in this paper.

Acknowledgements

This work was supported by Rolls-Royce plc. and funded by the Engineering and Physical Sciences Research Council (EPSRC), grant reference: EP/2522247/1. The authors also acknowledge the EPSRC for financial support of the Rigaku SmartLab via grants (EP/K009877/1), (EP/K00509X/1) and (EP/V035975/1).

Data availability

Data will be made available on request.

References

[1] J.H. Perepezko, The hotter the engine, the better, Science 326 (2009) 1068–1069.

[2] R.C. Reed, The superalloys: fundamentals and applications, Cambridge university press, 2008.

[3] T.M. Pollock, Alloy design for aircraft engines, Nat. Mater. 15 (2016) 809–815.

[4] L. Xu, Z. Sun, Q. Ruan, L. Xi, J. Gao, Y. Li, Development trend of cooling technology for turbine blades at super-high temperature of above 2000 K, Energies 16 (2023) 668.

[5] B.A. Pint, J.R. Distefano, I.G. Wright, Oxidation resistance: one barrier to moving beyond Ni-base superalloys, Materials Science Engineering A 415 (2006) 255–263.

[6] H. Long, S. Mao, Y. Liu, Z. Zhang, X. Han, Microstructural and compositional design of Ni-based single crystalline superalloys–A review, J. Alloy. Compd. 743 (2018) 203–220.

[7] J.L. Smialek, J.C. Schaeffer, C.A. Barrett, Design for Oxidation Resistance, in: Materials Selection and Design, 20, ASM Handbook, 1997.

[8] R. Darolia, Development of strong, oxidation and corrosion resistant nickel-based superalloys: critical review of challenges, progress and prospects, Int. Mater. Rev. 64 (2019) 355–380, https://doi.org/10.1080/09506608.2018.1516713.

[9] N. Birks, G.H. Meier, F.S. Pettit. Introduction to the High Temperature Oxidation of Metals, 2nd ed., Cambridge University Press, Cambridge, 2006 https://doi.org/10.1017/CBO9781139163903.

[10] J. Ma, W. Jiang, J. Wang, Y. Zhang, Z. Zhang, Initial oxidation behavior of a single crystal superalloy during stress at 1150 °C, Sci. Rep. 10 (2020), https://doi.org/10.1038/s41598-020-59968-3.

[11] S.J. Park, S.M. Seo, Y.S. Yoo, H.W. Jeong, H.J. Jang, Effects of Al and Ta on the high temperature oxidation of Ni-based superalloys, Corros. Sci. 90 (2015) 305–312, https://doi.org/10.1016/j.corsci.2014.10.025.

[12] C.M. Younes, G.C. Allen, J.A. Nicholson, High temperature oxidation behaviour of single crystal superalloys RR3000 and CMSX-4, Corros. Eng. Sci. Technol. 42 (2007) 80–88.

[13] M.H. Li, X.F. Sun, J.G. Li, Z.Y. Zhang, T. Jin, H.R. Guan, Z.Q. Hu, Oxidation behavior of a single-crystal Ni-base superalloy in air. I: at 800 and 900C, Oxid. Met. 59 (2003) 591–605.

[14] G.L. Erickson, A new, third-generation, single-crystal, casting superalloy, JOM 47 (1995) 36–39.

[15] A. Evangelou, Oxidation-fatigue mechanisms at moderate service temperatures in single crystal turbine blade materials, University of Southampton, 2017.

[16] K. Hariharan, M. Landes, M. Ramsperger, O. Luengas, T. Yu, E. Spiecker, C.H. Zenk, Y. Wang, S. Virtanen, High temperature oxidation of Ni-based superalloy 247 produced by electron beam powder bed fusion additive manufacturing, Corros. Sci. (2025) 113301.

[17] M. Arshad, S. Bano, M. Amer, V. Janik, Q. Hayat, Y. Huang, D. Guan, M. Bai, Thermodynamic insights into the oxidation mechanisms of CrMnFeCoNi high-entropy alloy using in situ x-ray diffraction, Materials 16 (2023) 5042.

[18] P. Shi, A. Engström, B. Sundman, Thermodynamic investigations on materials corrosion in some industrial and environmental processes, J. Environ. Sci. 23 (2011) S1–S7.

[19] P. Lukáš, L. Kunz, M. Svoboda, High-temperature ultra-high cycle fatigue damage of notched single crystal superalloys at high mean stresses, Int J. Fatigue 27 (2005) 1535–1540, https://doi.org/10.1016/j.ijfatigue.2005.06.006.

[20] K. Park, P. Withey, Compositions of gamma and gamma prime phases in an as-cast nickel-based single crystal superalloy turbine blade, Crystals 12 (2022) 299.

[21] A. Evangelou, K.A. Soady, S. Lockyer, N. Gao, P.A.S. Reed, Oxidation behaviour of single crystal nickel-based superalloys: intermediate temperature effects at 450–550° C, Mater. Sci. Technol. 34 (2018) 1679–1692.

[22] Y. Zhai, Y. Chen, Y. Zhao, H. Long, X. Li, Q. Deng, H. Lu, X. Yang, G. Yang, W. Li, Initial oxidation of Ni-based superalloy and its dynamic microscopic mechanisms: The interface junction initiated outwards oxidation, Acta Mater. 215 (2021) 116991.

[23] A. Akhtar, M.S. Hook, R.C. Reed, On the oxidation of the third-generation single-crystal superalloy CMSX-10, Metall. Mater. Trans. A 36 (2005) 3001–3017.

[24] H.P. Buwono, S. Adiwidodo, H. Wicaksono, H.I. Firmansyah, Hydrothermal synthesis and characterization of nano-particles γ-Al2O3, in: IOP Conf Ser Mater Sci Eng, IOP Publishing, 2021 012011.

[25] R.-S. Zhou, R.L. Snyder, Structures and transformation mechanisms of the η, γ and θ transition aluminas, Struct. Sci. 47 (1991) 617–630.

[26] L. del Campo, R.B. Pérez-Sáez, M.J. Tello, Iron oxidation kinetics study by using infrared spectral emissivity measurements below 570°C, Corros. Sci. 50 (2008) 194–199, https://doi.org/10.1016/j.corsci.2007.05.029.

[27] X.M. Wang, H. Liu, Y.Z. Hui, Z.Y. Yu, L. Li, C.H. Deng, Z.F. Yue, Quantitative study of the microstructure evolution along the thickness direction in the nickel-based single crystal superalloy DD6 at 1323 K thermal exposure, Mater. Charact. 154 (2019) 285–293.

[28] S. Yudin, A. Sedegov, D. Moskovskikh, S. Volodko, K. Kuskov, V. Suvorova, S. Danilova-Tretiak, S. Vorotilo, A. Nepapushev, A. Khort, Mechanism and kinetics of high-temperature oxidation of medium-and high-entropy carbides in air, Mater. Des. 231 (2023) 112048.

[29] T. Perez, D. Monceau, C. Desgranges, Kinetic oxidation model including the transient regime for a single crystal nickel-based superalloy over the temperature range 750–1300C, Corros. Sci. 206 (2022) 110485.

[30] S. Hamidi, M.R. Rahimipour, M.J. Eshraghi, S.M.M. Hadavi, H. Esfahani, Kinetics and microstructural investigation of high-temperature oxidation of IN-738LC super alloy, J. Mater. Eng. Perform. 26 (2017) 563–570.

[31] X. Zhuang, Y. Tan, X. You, P. Li, L. Zhao, C. Cui, H. Zhang, H. Cui, High temperature oxidation behavior and mechanism of a new Ni-Co-based superalloy, Vacuum 189 (2021) 110219, https://doi.org/10.1016/j.vacuum.2021.110219.

[32] N. Hussain, K.A. Shahid, I.H. Khan, S. Rahman, Oxidation of high-temperature alloys (superalloys) at elevated temperatures in air: I, Oxid. Met. 41 (1994) 251–269.

[33] C.L. Wagner, Contribution to the theory of the start-up process, J. Phys. Chem. 21B (1933) 25–41. 〈https://api.semanticscholar.org/CorpusID:99019671〉.

[34] H.A. Miley, Theory of oxidation and tarnishing of metals: I. The linear, parabolic and logarithmic laws, Trans. Electrochem. Soc. 81 (1942) 391.

[35] D.J. Young, M.J. Dignam, “Logarithmic” kinetics in thin film tarnishing, Oxid. Met. 5 (1972) 241–249, https://doi.org/10.1007/BF00609661.

[36] P.T. Landsberg, On the Logarithmic Rate Law in Chemisorption and Oxidation, J. Chem. Phys. 23 (1955) 1079–1087, https://doi.org/10.1063/1.1742193.

[37] H.T. Mallikarjuna, W.F. Caley, N.L. Richards, The dependence of oxidation resistance on gamma prime intermetallic size for superalloy IN738LC, Corros. Sci. 147 (2019) 394–405.

[38] J. Pei, Y. Li, C. Li, Z. Wang, Y. Liu, H. Li, Microstructure-dependent oxidation behavior of Ni-Al single-crystal alloys, J. Mater. Sci. Technol. 52 (2020) 162–171.

[39] G.L. Erickson, The development and application of CMSX-10, Superalloys 1996 (1996) 35–44.

[40] M. Hook, The effects of high temperature oxidation and exposure on nickel-base superalloys and turbine blade coatings, 2004.

[41] V.P. Sirotinkin, V.F. Shamrai, A.V. Samokhin, N.V. Alekseev, M.A. Sinaiskii, Phase composition of Al2O3 nanopowders prepared by plasma synthesis and heat-treated, Inorg. Mater. 48 (2012) 342–349.

[42] S.-H. Cai, S.N. Rashkeev, S.T. Pantelides, K. Sohlberg, Phase transformation mechanism between γ- and θ-alumina, Phys. Rev. B 67 (2003) 224104, https://doi.org/10.1103/PhysRevB.67.224104.

[43] K. Wefers, C. Misra, Oxides and hydroxides of aluminum, Alcoa Laboratories, Pittsburgh, PA, 1987.

[44] P.S. Santos, H.S. Santos, S.P. de Toledo, Standard transition aluminas. Electron microscopy studies, Mater. Res. 3 (2000) 104–114.

[45] S.V. Tsybulya, G.N. Kryukova, Nanocrystalline transition aluminas: Nanostructure and features of x-ray powder diffraction patterns of low-temperature Al 2 O 3 polymorphs, Phys. Rev. B 77 (2008) 024112.

[46] F. Pyczak, B. Devrient, H. Mughrabi, The Effects of Different Alloying Elements on the Thermal Expansion Coefficients, Lattice Constants and Misfit of Nickel-Based Superalloys Investigated by X-Ray Diffraction, Proc. Int. Symp Superalloys (2004), https://doi.org/10.7449/2004/Superalloys_2004_827_836.

[47] R. Völkl, U. Glatzel, M. Feller-Kniepmeier, Measurement of the lattice misfit in the single crystal nickel based superalloys CMSX-4, SRR99 and SC16 by convergent beam electron diffraction, Acta Mater. 46 (1998) 4395–4404, https://doi.org/10.1016/S1359-6454(98)00085-8.

[48] C. Schulze, M. Feller-Kniepmeier, Transmission electron microscopy of phase composition and lattice misfit in the Re-containing nickel-base superalloy CMSX-10, Materials Science Engineering A 281 (2000) 204–212, https://doi.org/10.1016/S0921-5093(99)00713-3.

[49] Q. Ding, Z. Shen, S. Xiang, H. Tian, J. Li, Z. Zhang, In-situ environmental TEM study of γ′-γ phase transformation induced by oxidation in a nickel-based single crystal superalloy, J. Alloy. Compd. 651 (2015) 255–258, https://doi.org/10.1016/j.jallcom.2015.07.017.

[50] D. Kubacka, M. Weiser, E. Spiecker, Early stages of high-temperature oxidation of Ni- and Co-base model superalloys: A comparative study using rapid thermal annealing and advanced electron microscopy, Corros. Sci. 191 (2021) 109744, https://doi.org/10.1016/j.corsci.2021.109744.

[51] J. Coakley, D. Ma, M. Frost, D. Dye, D. Seidman, D. Dunand, H. Stone, Lattice strain evolution and load partitioning during creep of a Ni-based superalloy single crystal with rafted γ ′ microstructure, Acta Mater. 135 (2017), https://doi.org/10.1016/j.actamat.2017.06.021.

[52] J. Ren, Y.-B. Hu, T.-S. Cao, C.-Q. Cheng, L. Zhang, J. Zhao, Unveiling the initial oxidation mechanism of a single crystal Ni-based superalloy with pre-deformation, Corros. Sci. 234 (2024) 112146.